Numerical study of two-phase flow dynamics and atomization in an open-type liquid swirl injector

Vishnu Natarajan[a], Umesh Unnikrishnan[b], Won-Sub Hwang[a], Jeong-Yeol Choi[a,*], Vigor Yang[b]

[a] *Department of Aerospace Engineering, Pusan National University, Busan, 46241, Republic of Korea*
[b] *School of Aerospace Engineering, Georgia Institute of Technology, Atlanta, GA 30332, USA*

ARTICLE INFO

ABSTRACT

The three-dimensional, two-phase flow dynamics and underlying physics in an open-type liquid swirl injector are investigated using numerical simulations. The basis for this study is a validated multiphase flow solver, interFoam, in OpenFOAM. Turbulence closure is achieved by means of LES with a one-equation eddy-viscosity turbulence model. A volume-of-fluid method is used for tracking the interface between the gas and liquid phases. The detailed spatio-temporal evolution of the flow field is explored systematically, including the liquid surface wave motion and liquid film characteristics within the injector, the helical air core, and the formation and atomization of the liquid spray cone downstream of the injector. The spectral content of the pressure field is also examined, to reveal the characteristic frequencies and feedback mechanisms of gas-liquid interactions.

1. Introduction

Liquid rocket engines (LREs) are an integral part of space exploration vehicles. In spite of the considerable progress made over the past eight decades, there remain many challenges in LRE design and development (Anderson and Yang, 1995; Harrje and Reardon, 1972). Combustion instability in particular presents important challenges and can have severe deleterious effects on engine operability.

Combustion instability results from the dynamic coupling between unsteady combustion and fluid dynamics in the engine (Culick and Yang, 1995). Fig. 1 schematically shows the interactions of the dynamic processes among the three major engine subsystems: propellant feed systems, injectors and combustion chamber (Kim, 2014).

Propellants pass through injectors from the feed system and undergo atomization, vaporization, and mixing in the combustion chamber. Pressure oscillations that develop in the combustion chamber affect injector characteristics such as propellant mass flow rate, which in turn causes unsteadiness in the combustion process and heat release. Injectors play a major role in the interactions between the feed system and the combustor (Bazarov and Yang, 1998; Chung et al., 2016; Kim, 2014). They not only facilitate the atomization and mixing of propellants, but also affect the stability and efficiency of the combustion device over the entire engine operation regime.

Swirl injectors provide good atomization quality and high mixing efficiency, and have been extensively used in practical LREs (Bazarov et al., 2004; Khavkin, 2004). They enable high flow rates, high thrust per injector element and superior throttling capability. Furthermore, since the flow passage in a swirl injector is relatively large, the atomization characteristics are less sensitive to manufacturing errors. The mean diameter of droplets is 2.2-2.5 times smaller than that produced by a jet injector with the same pressure drop and mass flow rate (Bazarov et al., 2004).

Swirl injectors can be classified into open and closed-type injectors according to their geometric configuration. A closed-type injector is equipped with an exit nozzle for improving the atomization quality through flow acceleration. An open-type injector, on the other hand, has a straight cylindrical chamber and offers better dynamic behavior (Bazarov et al., 2004). The manufacturing of open-type swirl injectors is much simpler than the manufacturing

---

* Corresponding author.
  E-mail address: aerochoi@pusan.ac.kr (J.-Y. Choi).

1. chamber internal process   2. liquid injection process   3. feed system process
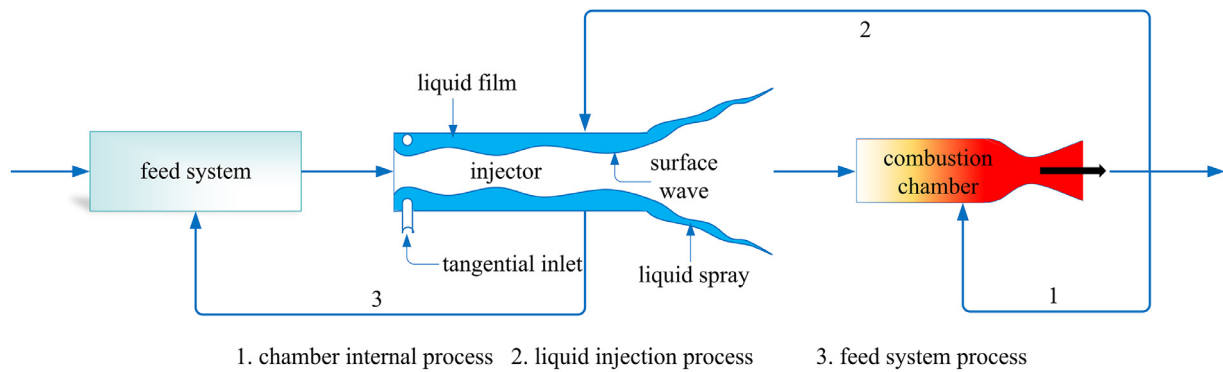
Fig. 1. Interactions of dynamic processes in LRE (Kim, 2014).

of closed-type swirl injectors. The dynamic characteristics of open-type swirl injectors have been studied theoretically and experimentally by Fu and co-workers (Fu et al. (2019), Fu et al. (2011a), Fu et al. (2011b), Fu et al. (2010) and Fu et al. (2012)). Their work has offered extensive insight into the underlying mechanisms and key parameters that dictate the injector performance and dynamics, and the results have been used to develop engineering design guidelines.

The fundamentals of inviscid swirl injector theory were established in the 1940s (Abramovich, 1944; Taylor, 1948). Extensive efforts were then made to achieve a thorough understanding of injector dynamics and flow physics over a wide range of injector geometries and operating conditions (Bazarov et al., 2004; Bazarov and Yang, 1998). The effects of vortex chamber geometry, nozzle length, injector flow rate, and pulsation magnitude on dynamic response characteristics were evaluated. Ismailov and Heister (2011a, 2011b) conducted linear and nonlinear analyses to study the dynamic response of swirl injectors. Both convergence and conical convergence resonance models were developed to investigate wave reflections and resonance behaviors. Chen and Yang (2014) recently examined the effects of ambient pressure on injector flow dynamics using a combined theoretical and numerical analysis.

A number of experiments have been carried out to study liquid swirl injector flow dynamics. Hulka and co-workers (Hulka and Makel (1993); Hulka and Schneider (1993); Hulka et al. (1991)) characterized the spray angle, circumferential spray uniformity, and drop size distribution of swirl coaxial injectors using pure water and water/nitrogen as working fluids. Hot fire testing was performed by Rahman et al. (1995) with a swirl coaxial injector using liquid oxygen (LOX) and gaseous hydrogen (GH2) as propellants. Visualization of near-injector swirling flames and LOX atomization was also conducted. Stable ignition and combustion were achieved for oxidizer-to-fuel ratios in the range of 3-166 and chamber pressure of 140-500 psia. Sasaki et al. (1997) conducted cold-flow and combustion tests at two different operating conditions. Both shear and swirl-coaxial injectors were investigated, with recessed and non-recessed LOX posts. Combustion efficiency was found to be limited by vaporization efficiency in the case of the shear-coaxial injector and mixing efficiency in the swirl-coaxial injector, respectively. An increase of heat load on the chamber wall and unstable combustion was observed in swirl-coaxial injectors.

Inamura et al. (2003) investigated theoretically liquid film development in a simplex swirl-coaxial injector. Empirical correlations for the sheet cone angle and breakup length were found to be applicable mainly inturbulent flows, and mismatch with measurements occurred when the liquid film transitioned from turbulent to laminar due to decreased flow rate. Im et al. (2005) car-

ried out self-pulsation experiments to study the spray and acoustic characteristics of a gas/liquid swirl-coaxial injector in the frequency range of 2–4 kHz. Liquid velocity appeared to be the only factor determining the acoustic frequency. Kim et al. (2007) measured the spray angle and breakup length using direct photography for different Weber numbers and pressures to investigate the spray and flow characteristics of a swirling liquid sheet. The maximum axial Weber number and ambient gas pressure were 1554 and 4.0 MPa respectively. The spray angle increased with increasing Weber number until the breakup of the liquid sheet. In addition, the breakup length decreased with increasing Weber number at high ambient pressure due to the effect of aerodynamic force. Kenny et al. (2009) investigated the behaviors of a liquid swirl injector by injecting water into gaseous nitrogen at a rate of 0.09 kg/s. The ambient pressure was varied in the range of 0.10–4.81 MPa. The shadowgraph technique was used to measure the film thickness and spray angle near the injector exit, whereas the film thickness upstream of the injector exit was measured using direct photography. The film thickness was found to increase with increasing ambient pressure, while the spray angle decreased. The underlying physics was explored in the combined theoretical and numerical study by Chen and Yang (2014). Moon et al. (2010) developed a sheet breakup model using linear stability theory and validated it against experimental data. Results indicated that liquid sheet breakup takes place in a long-wave regime at atmospheric conditions. The breakup mechanism switches to a short-wave regime at high pressures. Both experimental and computational results showed decrease in liquid-sheet breakup length and spray angle with increasing ambient pressure.

Kim et al. (2013) conducted cold-flow experiments to study the effects of recess length and momentum flux ratio on the spray patterns of gas-centered swirl-coaxial injectors. Water and gaseous nitrogen were used as working fluids. An increase in the momentum flux ratio led to a drastic change in the spray pattern from a wide hollow cone to a narrow solid cone. A high momentum flux ratio was required by the injector with shorter recess to maintain a spray pattern similar to that of a longer recess. Santolaya et al. (2013) measured droplet sizes and velocities using a phase Doppler particle analyzer. The spray patterns and droplet size distributions for a pressure swirl atomizer were examined. Chung et al. (2016) experimentally studied the flow dynamics of open-type swirl injectors with different geometries. The injector flow response to externally imposed pressure fluctuations was studied systematically for different geometries. The variation of the liquid film thickness was found to be proportional to the manifold pressure fluctuation. Such sensitivity decreased with decreasing swirl chamber length and diameter. Among the geometric parameters, the manifold diameter and tangential entry num-

Table 1
Multiphase flow studies on swirl injectors.

Author	Injector used	Interface capturing	Remarks
Dash et al. (2001)	Closed-type and open-type	VOF	Air core formation
Yeh (2007a, 2007b)	Plain-orifice atomizer, pressure-swirl atomizer	VOF	Performance evaluation of eddy viscosity and Reynolds stress models
Mandal et al. (2008)	Simplex atomizer	VOF	Power law and geometry effect on flow and atomizer performance
Fuster et al. (2009)	Single jet, co-flowing atomizer and swirl atomizer	Adaptive VOF	Different simulations of primary atomization
Renze et al. (2011)	Pressure-swirl atomizer	VOF	Spray pattern, pressure drop, and spray angle for non-Newtonian fluid
Nouri-Borujerdi and Kebriaee (2012)	Pressure-swirl atomizer	Level set	Simulations using an axisymmetric laminar and turbulent two-phase solver
Fu (2015)	Open-type	VOF	Effects of ambient pressure on internal flow
Galbiati et al. (2016a)	Pressure-swirl atomizer	VOF	Primary breakup and grid refinement study
Galbiati et al. (2016b)	Pressure-swirl atomizer	VOF	Effect of operating conditions and influence of turbulence models
Ding et al. (2016)	Pressure-swirl atomizer	VOF	Primary atomization
Shao et al. (2017)	Annular swirling jet	Mass conservative level set	Swirl and atomization characteristics with influence of turbulent flow
Cheng et al. (2018)	Pressure-swirl atomizer	VOF	Response to ramp variation of mass flow rate
Laurila et al. (2019)	Pressure-swirl atomizer	geometric VOF	Inner nozzle flow and liquid sheet instability for high viscosity fluids and instability for Re from 420-5300
Bai et al. (2020)	Liquid-centered swirl coaxial injector	VOF with CICSAM	Self-pulsation characteristics with different annulus width and post thickness
Laurila et al. (2020)	Pressure-swirl atomizer	geometric VOF	Comparison between computational and experimental investigations, inner nozzle and near-field flow characteristics
Present study	Open-type	VOF	Investigation of flow field inside the injector and primary atomization

ber had greater impact, compared with the length and diameter of the swirl chamber.

A number of numerical studies have been carried out on swirl injectors. Wang and colleagues (Wang et al. (2001); Wang et al. (2007)) investigated gas-turbine swirl injector flow dynamics using large eddy simulations (LES). Zong and Yang (2008) studied the flow dynamics of a swirl injector under supercritical conditions The interactions of hydrodynamic instabilities and acoustic oscillations in the injector were examined in detail. Huo et al. (2009) studied the response of swirl injector flows to external forcing at supercritical conditions over a wide range of frequency. Fuster et al. (2009) conducted simulations of primary atomization in several swirl atomizers using an adaptive VOF method. Siamas et al. (2009) explored the dynamics of annular gas-liquid two-phase swirling jets. Two computational cases with different gas-liquid density ratios were considered. Nouri-Borujerdi and Kebriaee (2012) simulated laminar and turbulent flows in a pressure swirl atomizer using an axisymmetric two-phase solver along with a level-set method for interface capturing. Wang and co-workers (Wang et al. (2017a); Wang et al. (2015)) performed three-dimensional analyses of supercritical fluid dynamics in swirl injectors. Fu (2015) conducted axisymmetric flow simulations of open-end swirl injectors with and without pressure oscillations. The effect of turbulence on spray characteristics was investigated and compared with experimental data from Elbadawy et al. (2015). Recently, comprehensive numerical studies using LES techniques were carried out to explore detailed flow dynamics in liquid oxygen/kerosene bi-swirl injectors (Wang et al., 2017b) and gas-centered liquid-swirl coaxial injectors (Wang et al., 2019; Zhang et al., 2018) under supercritical conditions. Table 1 lists multiphase flow studies on liquid swirl injectors.

Until now, most of the numerical studies on multiphase injector flow dynamics have been carried out using closed-type swirl geometries. Open-type swirl injectors have been investigated mainly using experimental techniques. As a result, detailed flow structures within injectors have not been well understood. The present work

attempts to study the complex flow dynamics inside an open-type swirl injector by performing multiphase flow simulations. Formation and evolution of the air core, liquid-film development, and primary atomization characteristics are treated in detail. The spectral attributes and characteristic acoustic frequencies of the flow field are also quantified.

2. Numerical approach

The interFoam solver in OpenFOAM is employed to perform multiphase flow simulations in this study. The code deals with transient, incompressible, isothermal, multiphase flows with immiscible fluids. The interface between two fluids is captured by means of a volume-of-fluid (VOF) method.

2.1. Governing equations

The continuity equation is given by

$$\nabla . (\vec{U}) = 0 \tag{1}$$

$$\vec{U} = \alpha \vec{U}_l + (1 - \alpha) \vec{U}_g \tag{2}$$

where α is the volume fraction of the liquid phase in a cell, ranging from 0 to 1. The subscripts l and g denote the liquid and gas phases, respectively. A cell completely filled with liquid is represented by $\alpha=1$ and the gaseous phase is indicated by $\alpha=0$. A value between 0 and 1 represents the interface between the liquid and gaseous phases.

The fluid properties at any point in the domain are calculated as the volume fraction-weighted average of the corresponding properties of the two fluids. Thus, for example, the fluid density at a given point in space is computed as,

$$\rho = \alpha \rho_l + (1 - \alpha) \rho_g \tag{3}$$

The momentum equation is

$$\frac{\partial \rho \vec{U}}{\partial t} + \nabla . \left(\rho \vec{U} \vec{U} \right) = -\nabla P + \nabla . T + \rho \vec{F}_b \tag{4}$$

T in Eq. (4) is the deviatoric stress tensor where the stress term can be expressed as follows for an incompressible flow.

$$T = 2\mu S \tag{5}$$

$$\mu = \alpha \mu_l + (1 - \alpha)\mu_g \tag{6}$$

where μ is the laminar molecular viscosity and S is the mean rate of strain tensor defined as $S = 0.5[\nabla \vec{U} + (\nabla \vec{U})^T]$. For Newtonian and incompressible flows, the stress term in Eq. (4) can be further decomposed with the aid of the identity of the divergence operation in vector calculus.

$$\nabla . T = \nabla . \left(\mu \nabla \vec{U} \right) + \nabla \vec{U} . \nabla \mu \tag{7}$$

F_b in Eq. (4) is the body force term consisting of gravity and surface tension. The latter is evaluated using the Continuum Surface Force (CSF) model as

$$\vec{F}_\sigma = \sigma \kappa \nabla \alpha \tag{8}$$

where σ is the surface tension constant and κ is the mean curvature of the free surface, obtained from the following relation

$$\kappa = -\nabla . \hat{n} = -\nabla . \left(\frac{\nabla \alpha}{|\nabla \alpha|} \right) \tag{9}$$

where $\hat{n}$ is the interface unit normal vector. It is common to use a modified pressure in the VOF method for convenience in applying boundary conditions for pressure. The modified pressure is given as

$$P_d = P - \rho \vec{g} . \vec{x} \tag{10}$$

where $\vec{g}$ and $\vec{x}$ denote acceleration due to gravity and the position vectors in Cartesian coordinates, respectively. Using Eqs. (5)–(10), Eq. (4) can be re-written for a two-phase, Newtonian, incompressible flow as

$$\frac{\partial \rho \vec{U}}{\partial t} + \nabla . \left(\rho \vec{U} \vec{U} \right) - \nabla . \left(\mu \nabla \vec{U} \right) - \nabla \vec{U} . \nabla \mu$$
$$= -\nabla . P_d - \vec{g} . \vec{x} \nabla \rho + \sigma \kappa \nabla \alpha \tag{11}$$

The phase continuity equation is

$$\frac{\partial \alpha}{\partial t} + \nabla . \left(\vec{U} \alpha \right) = 0 \tag{12}$$

The appropriate modeling of tubulence remains one of the great questions of fluid dynamics. Modeling of single-phase flows is a complex topic in itself; turbulence in multiphase flows is even more intricate (Kolev, 2012). Near the interface between fluids, the turbulence structures become anisotropic, andin immiscible fluids, the interfacial turbulence may incorporate various types of breakup and reformation of the boundaries, including vortex interactions, rapid deformations, and ligament formation (Shirani et al., 2006). A robust modeling framework for multiphase turbulent flows is still an open research question. In recent decades, with increases in computational power, LES has become an attractive approach for turbulence modeling (Balabel, 2012). The LES technique, along with the one-equation eddy viscosity subgrid model (Kim and Menon, 1995), is adopted for turbulence closure in our study. The one-equation subgrid model uses the eddy viscosity approximation, where the subgrid-scale stress tensor τ_{ij} is approximated as follows:

$$\tau_{ij} \approx \frac{2}{3} k_{sgs} \delta_{ij} - 2\nu_{sgs} dev\left(\overline{D} \right)_{ij} \tag{13}$$

Here ν_{sgs} is the subgrid-scale eddy viscosity, $\overline{D}$ is the resolved-scale strain rate tensor defined as

$$\overline{D}_{ij} = \frac{1}{2} \left(\frac{\partial \overline{u}_i}{\partial x_j} + \frac{\partial \overline{u}_j}{\partial x_i} \right) \tag{14}$$

and the subgrid-scale kinetic energy k_{sgs} is

$$k_{sgs} = \frac{1}{2} \tau_{kk} = \frac{1}{2} (\overline{u_k u_k} - \overline{u}_k \overline{u}_k) \tag{15}$$

The subgrid scale eddy viscosity ν_{sgs} is computed using k_{sgs} as

$$\nu_{sgs} = C_k \sqrt{k_{sgs}} \Delta \tag{16}$$

where Δ is the local grid (filter) size and C_k is a model constant whose default value is 0.094. The difference between the Smagorinsky model (Smagorinsky, 1963) and the one-equation eddy-viscosity model lies in the computation of k_{sgs}. The Smagorinsky model assumes local equilibrium to compute k_{sgs} whereas the one-equation eddy viscosity model solves a transport equation for k_{sgs} as follows

$$\frac{\partial (\rho k_{sgs})}{\partial t} + \frac{\partial (\rho \overline{u}_j k_{sgs})}{\partial x_j} - \frac{\partial}{\partial x_j} \left[\rho (\nu + \nu_{sgs}) \frac{\partial k_{sgs}}{\partial x_j} \right]$$
$$= -\rho \tau_{ij} : \overline{D}_{ij} - C_\in \tag{17}$$

where the operator : denotes a double inner product, ρ is the density, ν is the kinematic viscosity and $C_\in$ is another model constant.

The governing equations are discretized using the finite volume method (FVM) on an unstructured grid. A second order implicit, bounded Crank Nicolson scheme is applied for time integration. The Gauss linear interpolation is implemented for interpolation of values from cell centers to face centers for the gradient computations. Linear interpolation is used for the computation of divergence terms, except for the divergence of φ (where φ is flux across cell faces) and α, for which the van Leer limiter is used. The PISO (Pressure Implicit with Splitting of Operators) algorithm is employed for coupling the momentum equations with the mass conservation equation. A preconditioned conjugate gradient (PCG) solver is used along with the diagonal incomplete-Cholesky (DIC) preconditioner for the pressure term and a smooth solver with Gauss-Seidel smoother is used for solving all the other terms.

2.2. Injector configuration and boundary conditions

Fig. 2 shows a schematic of the three-dimensional open-type swirl injector considered in the present study along with the unstructured grid system. The injector consists of three inlets each of 1.4 mm diameter and 5 mm length, which inject water tangentially into the swirl chamber. The swirl chamber is 7 mm in diameter and 55 mm long. An exterior domain, which is 30 mm in diameter and 30 mm long, is included at the exit of the injector, to enable examination of the liquid spray and flow field characteristics downstream of the injector. The top surface of the injector is modeled as a solid wall and the no-slip boundary condition is assigned to it and all other injector walls. For the exterior domain boundary, an outflow boundary condition through which flow can pass is prescribed. The exterior domain and injector are initialized with air at zero velocity and atmospheric pressure. Water is injected through the tangential inlets at a total flow rate of 90g/s and the pressure difference across the injector is set to 6.0 bar. The dimensions of the geometry and the boundary conditions were chosen to match the experimental study of Kim (2014).

The unstructured grid comprises tetrahedron cellsof sizes ranging between 15-125 μm. The finest cells are located within the injector and in its vicinity, and the cells are coarsened in the exterior domain. The time step size is calculated at every iteration
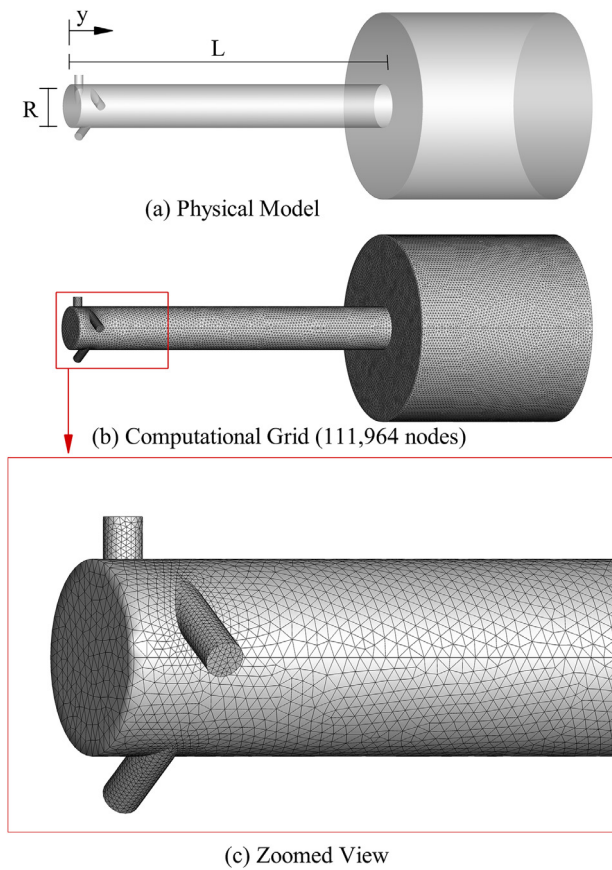
(a) Physical Model

(b) Computational Grid (111,964 nodes)

(c) Zoomed View

Fig. 2. Schematic of an open-type swirl injector and the computational mesh. (Coarse mesh is shown for clarity).

Table 2
Film thickness values for four mesh resolutions and experimental result

Type	No. of Nodes	Film Thickness, mm
Experimental result (Kim, 2014)	-	1.29
Coarse mesh	111,964	2.24
Medium mesh	590,857	1.66
Fine mesh	3,523,955	1.21
Very Fine mesh	6,554,640	1.20

with a maximum Courant number of 1.0. The computational domain is decomposed into 288 subdomains using the Scotch decomposition method and the decomposed case is run using MPI. The flow-through time, defined as the time taken for the flow to reach the injector exit, is around t = 10 ms, and the simulation is further run until t = 20 ms to ensure that the flow is fully developed and has reached a steady state.

2.3. Model validation and grid convergence study

The performance of the interFoam solver used in our study was investigated in detail by Deshpande et al. (2012). They found that the solver is capable of capturing flow physics reasonably well even with modest grid resolution for simulation of liquid sheet atomization. In their work, they evaluated the liquid crown diameter and showed excellent agreement with experimental work (Cossali et al., 1997), proving the validity of the interFoam solver.

In this paper, we present a validation test based on film thickness values compared against the experimental results of Kim (2014). The validation is performed at three levels of mesh resolution, with increasing node or cell counts, as listed in Table 2. The pressure, liquid film thickness, and the interface dynamics be-
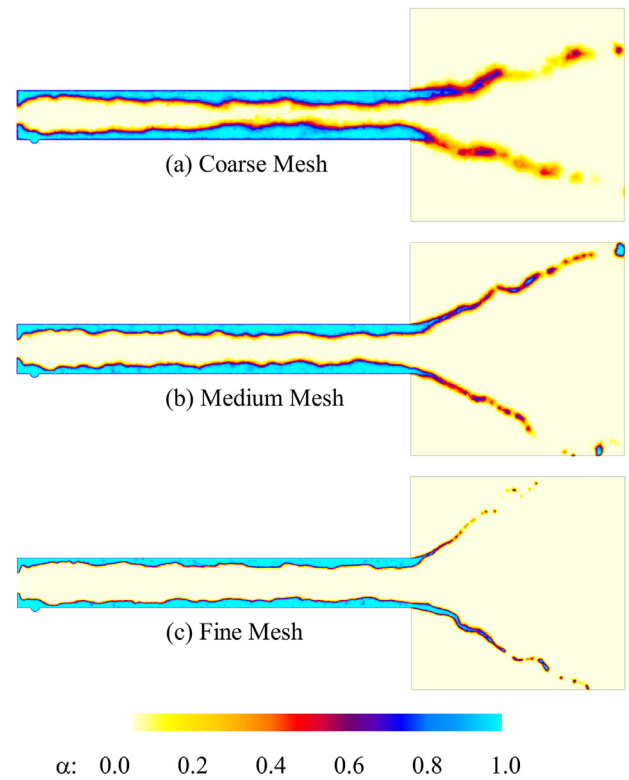

(a) Coarse Mesh

(b) Medium Mesh

(c) Fine Mesh

α: 0.0   0.2   0.4   0.6   0.8   1.0

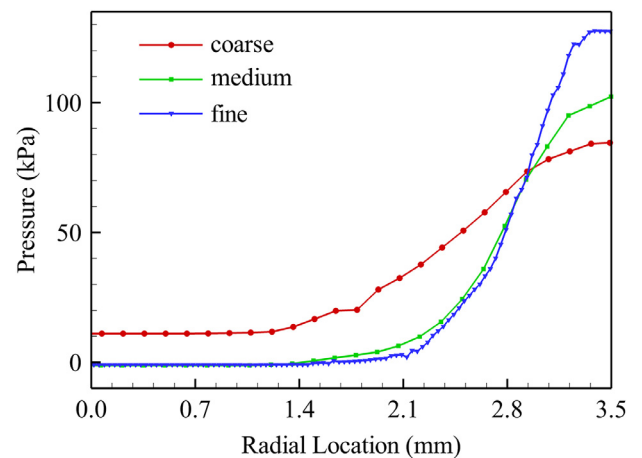**Fig. 3.** Liquid-volume-fraction contours for three different mesh resolutions

Fig. 4. Radial pressure profiles at the injector exit (y/L = 1.00) at t = 20 ms for three mesh resolutions.

tween water and air, which are the main considerations for our investigation, are examined for model validation and grid convergence. Fig. 3 shows the liquid-volume-fraction contours in the injector at time t = 20 ms for the three different mesh resolutions. It is clear that the interface becomes more distinct as the cell size decreases. The thickness of the film is higher and the interface is smeared with the coarse mesh. As the mesh is refined, the interface becomes sharper and the wavy structure of the flow field becomes more distinct.

The variation of instantaneous pressure at time t = 20 ms along a radial position is shown in Fig. 4 for the three mesh levels. The pressure profiles are taken at a radial line at the injector exit (y/L = 1.00) at time t = 20 ms. It is seen that the medium and
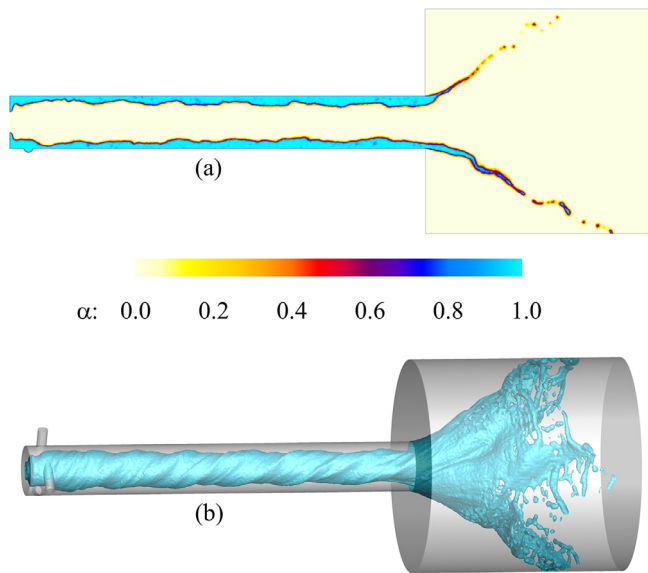
Fig. 5. Snapshots of (a) liquid-volume-fraction contour along a longitudinal section and (b) iso-surface contour for liquid-volume-fraction, $\alpha = 0.25$.

Fig. 6. Liquid-volume-fraction contour at various streamwise locations inside the injector from t = 18 ms to t = 20 ms with $\Delta t = 1$ ms.

fine mesh cases show very similar profiles, but since the interface tracking is sharper in the fine mesh, we use the fine mesh here.

The film thickness at the exit of an injector characterizes the injector performance; here here we calculate film thickness as the radial distance from the wall at which $\alpha = 0.1$ (recall that α is the volume fraction of the liquid phase in a cell). Film thickness varies over time and, corresponding to pressure, it varies at different circumferential locations inside the injector. Therefore film thickness is measured at the injector exit (y/L=1.00) at different circumferential locations and different time instants, and the mean values (averaged over both circumference and time) are tabulated. Table 2 details the mean film thickness values corresponding to the three mesh resolutions, and the experimental result. The computed results more closely match the measured film thickness value closely as the mesh is refined. The error in the calculated film thickness is only 6.43% for the fine mesh.

To check whether a finer mesh would produce an even lower film thickness value, another case with a larger number of nodes was tested. It can be seen from Table 2 that the film thickness value does not decrease much further with the Very Fine mesh. This is because the decrease in cell size and the corresponding change in interface position happens within a few micrometers. Therefore, the change in film thickness with further decrease in mesh size is also of the order of few micrometers. This result justifies, qualitatively and quantitatively, that the fine mesh model with the current solver and choice of numerical schemes is sufficient to capture the three-dimensional flow dynamics and the multiphase flow interface at the desired level of accuracy.

3. Results and discussion

3.1. Instantaneous flow fields

Fig. 5a shows a snapshot of the liquid-volume-fraction distribution along a longitudinal cut section. The thickness of the film varies in an uneven manner along the length of the swirl chamber. Regions of alternating low and high film thickness gives the liquid film a wavy structure. The thickness of the film is inversely proportional to the axial velocity of the flow in the swirl chamber. In the open-type swirl injector, there is no convergent sec-
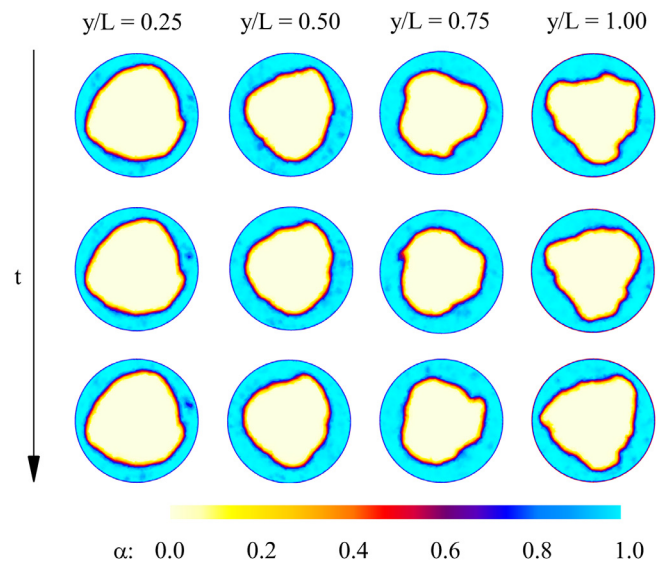
tion at the end of the injector and so there is no acceleration of the flow due to the change in injector shape, and the liquid film thickness of the open-type swirl injector is slightly higher than that of an equivalent closed-type injector. Hydrodynamic instabilities are also present inside the swirl chamber. The iso-surface contour of the liquid-volume-fraction is used to visualize the three-dimensional structure of the liquid film inside the swirl injector. Fig. 5b presents a snapshot of the iso-surface contour for $\alpha = 0.25$, which is almost at the end of the transition region from water to air, that is the interface between water and air. This illustrates the helical path of the swirling flow inside the swirl chamber along with the conical spray formed outside the injector. The liquid is injected tangentially and the centrifugal force associated with the swirling motion causes the liquid to swirl along the injector wall, while the region inside the liquid vortex is filled with ambient gas. The swirling motion within the injector increases the flow residence time compared to that of a jet injector, and has several advantages from a mixing standpoint. A significant portion of the acoustic energy from the combustion chamber is withdrawn into the gas manifold, and the gas cavity acts as an acoustic resonator (Long et al., 2003). Since the air core formed at the center of the swirling flow in the swirl chamber acts as an acoustic damper, the pressure fluctuations generated in the combustion chamber do not easily propagate from the combustion chamber to the feed system and vice versa (Bazarov, 1996). Since there is no convergent section downstream, there will also not be reflected waves as in the case of closed-type swirl injectors. Outside the injector, the flow forms a conical sheet, which breaks up into ligaments and eventually into small droplets. These phenomena are examined in more detail in Section 3.3.

3.2. Flow field inside the injector

3.2.1. Overview

Fig. 6 depicts the variation of liquid-volume-fraction at various streamwise locations inside the swirl injector at different time intervals. The snapshots are taken from t = 18 ms to t = 20 ms with a time interval of 1 ms between snapshots. Although the flow is swirling within a circular chamber, the developed liquid film surface inside the injector is not circular. Near the head end of the injector, the liquid film surface is relatively smooth with a small film thickness value. The film thickness increases as we go down-
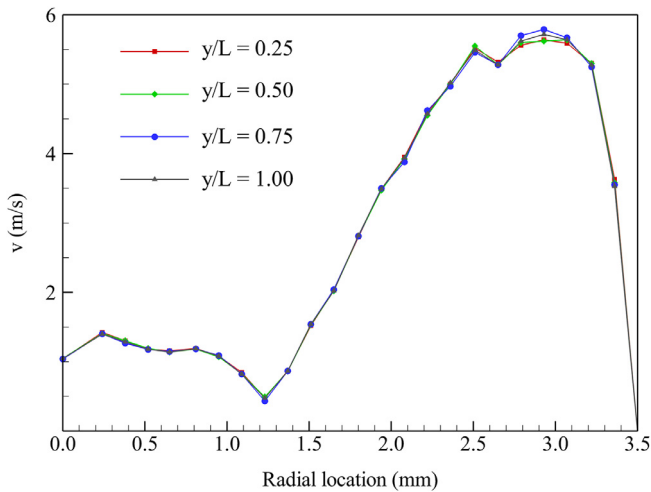
Fig. 7. Circumferentially-averaged tangential velocity profile along the radius at different axial locations of the injector at t = 20 ms.

Fig. 8. Flow streamlines from the three tangential inlets.

Fig. 9. Air core formation inside the swirl injector, helical striation waves - 1, 2, 3.

stream, except at the injector exit where it is relatively smaller. The contours at y/L = 1.00 show a smaller film thickness compared to the contours at y/L = 0.75 due to the variation of the axial fluid velocity along the length of the chamber. In general, the film thickness increases as the axial velocity decreases. Initially, near the injector head, the axial velocity is comparatively small, since the flow is injected in the tangential direction. Due to wall friction, the axial velocity decreases further, causing the liquid film thickness to be higher at y/L = 0.5 and y/L = 0.75. Near the injector exit, the axial velocity increases as the static pressure induced by the swirling motion is converted into axial acceleration (Chen and Yang, 2014), and therefore the liquid film thickness is relatively lower at y/L = 1.00, as shown by the contours in Fig. 6. The circumferential waviness in the film surface also intensifies as we move from the injector head end to the exit. The variation in film thickness implies that the shape of the central air core has changed. The radius of the air core is an important parameter that determines the film thickness and average drop size in the process of atomization (Som and Mukherjee, 1980). In addition to the variation in the streamwise and circumferential directions, the film thickness also varies in time. The temporal changes in the film thickness near the head end are minimal, whereas the fluctuations become more prominent downstream along the length of the swirl chamber.

The circumferentially-averaged tangential velocity profile is plotted along the radius at four different axial locations of the injector at t = 20 ms in Fig. 7. It is seen that the profiles are almost identical in all the locations, although there is a slight difference in the peak values. The peak velocity is highest at y/L = 0.75, followed by y/L = 1.00. The effect of the wall region is also seen in these profiles. The air core region is almost stagnant, although low velocity flow is present. Even at the center the velocity is not exactly zero. as the flow does not swirl exactly around the geometric center. The velocity increases as we move into the liquid film toward the wall, and then decreases again at the wall. The swirling motion of the liquid and resulting viscous stress at the liquid-air interface force the air close to the liquid film surface to move along with it, and this gives the stagnant air inside the chamber a small velocity. The tangential velocity in the circumferential direction also varies. Due to non-uniform tangential velocity, the liquid film inside the swirl chamber is also non-uniform and non-circular, as seen in Fig. 6. The variation of film thickness and velocity fluctuations affect the primary breakup of the conical liquid spray.
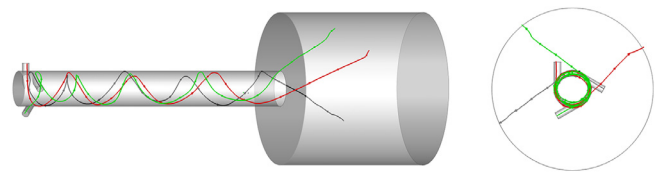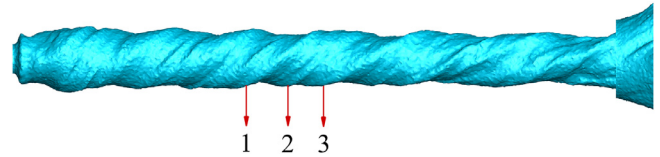
3.2.2. Streamlines

A three-dimensional visualization of streamlines from each of the three tangential inlets along with the top view of the streamlines is shown in Fig. 8. The streamline characteristics vary along the swirl chamber. The streamlines do not remain equidistant and do not even follow similar paths inside the chamber. The relative distance between the streamlines and the helical angle of the swirling flow increase along the swirl chamber, causing the streamlines to spread apart. The helical flow path along with the increase in the helical angle can be seen in Fig. 8. The streamlines of the velocity field indicate that the flow spreads further after exiting the swirl chamber. At the injector exit, the streamlines are discharged at different angles with respect to each other. The relative angles between the streamlines at the exit are significantly different from the initial angle between them (120^0) at the start of injection, and the streamlines also have a larger helical angle outside the injector.

3.2.3. Air core and surface waves

A fully developed helical air core formed inside the injector is visualized in Fig. 9. This corresponds to the iso-surface contour at $\alpha = 0.25$. An air core is formed when the centrifugal force of the swirling flow inside the injector dominates the viscous force. Due to the centrifugal motion of the liquid, a low pressure area is created near the injector exit which entrains ambient air into the injector (Amini, 2016). Thus, formation of an air core inside the injector depends on the presence of sufficient inlet velocity or flow rate (Dash et al., 2001). The average diameter of the air core computed from our study is around 4.58 mm, and the core is not symmetrical about the center of the swirl chamber.

The surface waves developed over the air core are also seen in Fig. 9. These waves influence the liquid film characteristics at the injector exit, which in turn affect the atomization process. The air core inside the swirl chamber reveals the presence of edges or striations, which are formed due to the flow from the three inlets. A triple helix shape is formed, rotating in the same direction as the liquid swirl inside the chamber. This is in agreement with the results of Chinn et al. (2016), who reported that the number of edges in the helical air core is equal to the number of tangential inlets that feed the flow into the chamber. Two of these edges are very sharp and one edge is somewhat blunt. It is also seen from Fig. 9 that the distance between the air core edges increases as we move toward the injector exit. The axis of the air core is not exactly aligned with the center of the swirl chamber but is rather slightly off-center of the central axis of the chamber. The air core formed inside the injector along with the liquid flow swirling
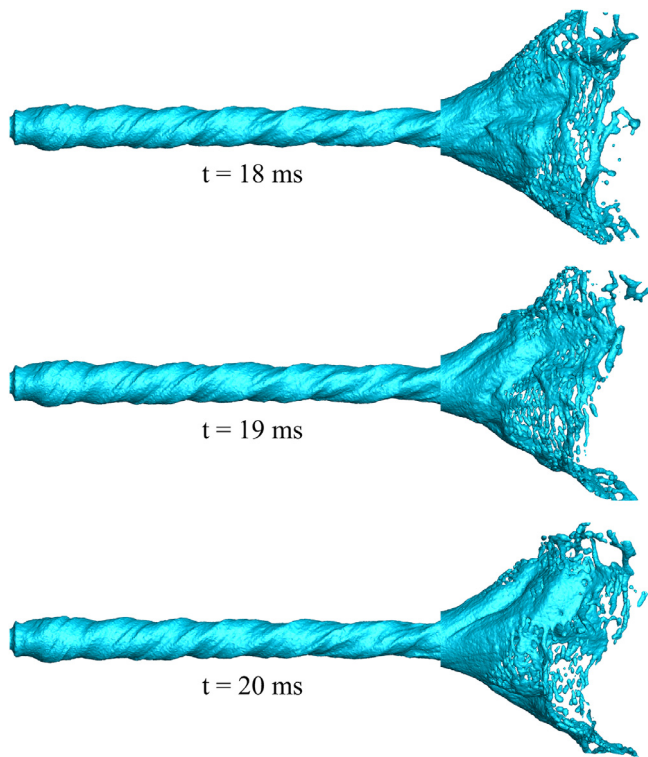
Fig. 10. Variation of iso-surface contours at different time instants for liquid-volume-fraction, $\alpha = 0.25$.

Fig. 11. Primary breakup process and droplet formation in the conical spray. a) disturbance waves, b) ligament formation, c) fluid thread breakup by pinching, d) primary breakup, e) secondary breakup (small droplet).

around the chamber, act as a damper for the pressure fluctuations propagating from the combustion chamber to the feed system and vice versa. Therefore, the shape and size of the air core play an important role in the dynamics of the injector.

3.3. Flow field outside the injector

3.3.1. Spray characteristics

The temporal variation of the liquid-air interface represented by the iso-surface contour for α=0.25 is shown in Fig. 10. Since there is no acceleration of the flow due to the injector shape in an open-type swirl injector, the liquid sheet breakup length is larger than in an equivalent closed-type swirl injector. The liquid spray is almost conical and hydrodynamic waves are observed on the conical surface. Primary breakup of the liquid sheet occurs due to growth of these unstable waves at the interface between the water and air. The breakup length is found to vary around the conical spray due to the variation of film thickness in the circumferential direction inside the injector. A droplet is formed when the turbulent fluctuations in the liquid jet have sufficient momentum to overcome the surface tension force (Wu et al., 1991; Wu et al., 1992). Most of the droplets formed after primary breakup are irregular in shape or like elongated ellipsoids, although a few spherical or ovoid droplets are also seen after secondary and tertiary breakup. Droplets are formed more promptly in regions where the film thickness is small, and there is a delay in droplet formation when the film thickness is high. The droplets formed are larger in size when the film thickness is higher, while finer droplets are obtained in regions where there is smaller film thickness.

3.3.2. Spray cone angle and Weber number

The conical liquid sheet formed in the exterior domain has a non-uniform spray angle due to the velocity variation in the circumferential direction inside the swirl injector. The spray cone angle is measured fro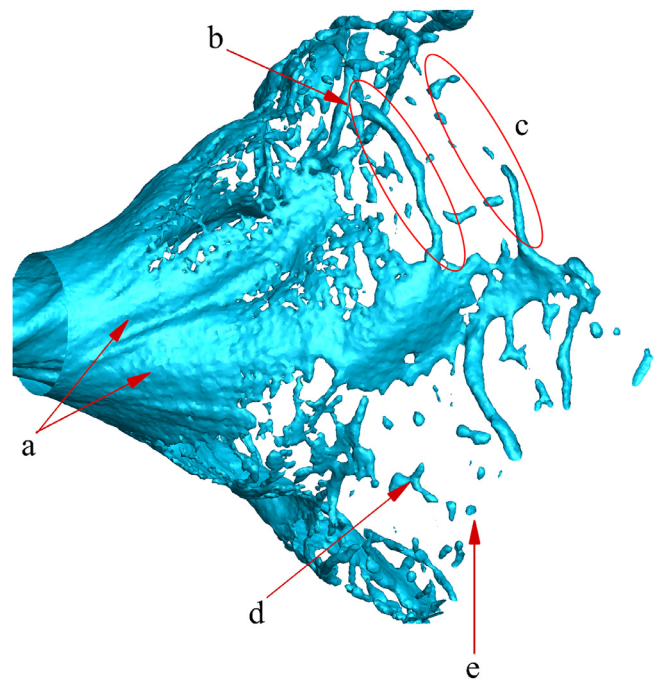m our simulation at different cut sections for different time intervals. The estimated mean spray cone angle is about 61 degrees, and it varies by +/- 8 degrees around the conical spray. The cone angle is higher in regions of smaller film thickness due to the higher tangential velocity, and lower in regions of larger film thickness.

The balance of deforming (inertial) and restoring (surface tension) forces acting on the liquid film govern the disintegration of the liquid film into fragments. This balance can be described using the Weber number, a dimensionless number that quantifies the ratio of inertial force to the surface tension force. The Weber number is given by,

$$We = \frac{\rho v^2 D}{\sigma} \qquad (18)$$

For the present case, the Weber number is equal to 7595.92. This implies that the inertial force is much larger than the surface tension force. The surface waves are more turbulent and the flow is more likely to deform into droplets as it reaches the injector exit.

3.3.3. Atomization

The atomization processes inside the swirl injector are explained in more detail with the help of Fig. 11, which shows the iso-surface contour obtained for $\alpha = 0.5$. The liquid emerges from the injector as a swirling sheet, and several processes promote its eventual breakup into droplets. Since the flow is swirling radially outwards, the film becomes thinner, and breaks into ligaments, and these ligaments further break up into droplets through Rayleigh instability. The swirling motion of the jet also supports the breakdown into droplets and liquid threads. The ligaments formed are not uniform in size, and there is a significant difference in ligament size based on the thickness of the liquid film. The droplet sizes in turn depend on the size of the ligament from which they are formed. Furthermore, as noted earlier, the liquid film thickness varies around the circumference of the spray at the injector exit, so surface waves form on the spray cone starting from the nozzle exit. These waves grow as they propagate downstream and foster breakup into droplets. Disturbance waves also form on the spray
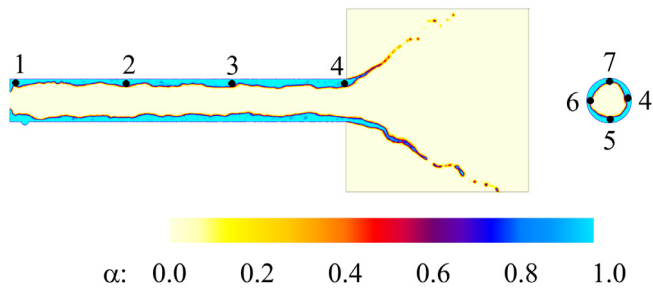
Fig. 12. Probe locations for data acquisition inside the injector.

surface, promoting the breakup of the liquid film into droplets. The breakup processes are not all internal to the spray; aerodynamic forces exerted by the surrounding air also support liquid sheet breakup.

The process by which the liquid film or ligament breaks up into droplets is called the primary breakup process. The liquid breakup length is defined as the distance up to which the liquid film stays connected with the injector. This is an important parameter in the study of atomization characteristics as it defines the spatial extent of the primary atomization region (Charalampous et al., 2016). The average vertical breakup length is estimated in this case as 18.94 mm. In some regions, the primary droplets are formed quickly, while in some regions we only observe partial disintegration of the liquid film within the set domain length. The droplet size variation in the conical spray is also indicated somewhat generally in Fig. 11, where larger and smaller droplets are clearly visible after primary breakup. Downstream of this region, these droplets further breakup into smaller droplets during the secondary breakup process, and coalescence may also occur. The circumferential variations in the breakup length and droplet formation are minimal compared to other injector configurations, and the spray pattern is almost uniform(an advantage of open-type injectors).

3.4. Spectral analysis

In this section, we investigate the spectral dynamics of the swirl injector quantitatively using the fast Fourier transform (FFT). To perform FFT, flowfield data are collected at various probe locations along the longitudinal and circumferential locations inside the swirl injector. The probe locations identified for our analysis are shown in Fig. 12. Data was collected after the flow was fully developed and had reached a quasi-steady state, from t = 15 ms to t = 20 ms, with a sampling time interval of 1×10^{-7} s. The grid convergence study conducted earlier (Section 2.3) was based on the pressure value inside the injector. So the pressure fluctuations from the fine grid are considered to be converged and accurate for

our analysis. To verify the validity and sufficiency of the sampling frequency, we extracted data from probe 1, which is near the top surface of the injector, with different sampling times. FFT was performed using data corresponding to each sampling time step, and the results obtained are shown in Fig. 13. It is seen that the peak frequency, defined as the frequency at which the power spectral density (PSD) reaches a maximum value, and the corresponding magnitudes of PSD, are the same for all time step sizes considered. Based on this finding, we used the sampling time step 1×10^{-07} s for the remainder of the analyses. The present spectral analysis can be considered accurate, based on the sampling time step size and the grid resolution.

Fig. 14 shows plots of pressure fluctuations for probe locations 1-4, positioned along the longitudinal direction of the injector. The plot shows the variation of p'/p (%) with time, where the instantaneous pressure fluctuation p' is normalized by the time-averaged pressure p. The pressure oscillations are periodic near the head end of the injector and become more intermittent and irregular as we move downstream closer to the injector exit. The corresponding PSD of the pressure fluctuations are shown in Fig. 15. It is seen that at probe 1, which is closest to the injector head, there is a peak value of PSD at a frequency of about 40 kHz. As we move downstream towards the injector exit, this peak drops, and we observe several peaks at high frequencies, perhaps due to the instability or disturbance waves that emerge over the liquid film surface. The overall peak values of PSD, however, decrease. In addition, the peak frequencies change. As we move n closer to the injector exit, we observe that the high frequency peaks diminish and a low frequency peak in the range of 2-3 kHz becomes prominent. At the injector exit, the peak frequency is about 2 kHz. The maximum PSD values drop by four orders of magnitude along the injector. From these observations, it is inferred that high frequency pressure oscillations damp out as we move toward the injector exit, and are replaced by a low frequency mode. This low frequency oscillation mode could have an important effect on the subsequent liquid sheet breakup and atomization processes.

The pressure fluctuation-time history plots for probes 4-7, located circumferentially at the exit of the injector (y/L = 1.00) are shown in Fig. 16, and the corresponding PSD are presented in Fig. 17. The variation in the behavior of the pressure oscillation in the circumferential direction is evident. The 2 kHz peak observed at probe 4 is not found at other circumferential locations. In fact, multiple peaks are observed in the frequency range between 2-8 kHz. At probe 6, a peak at slightly higher frequency in the range of 31.5 kHz is also observed. The high frequency mode oscillations at the injector exit are obtained in regions where the time-averaged film thickness value is comparatively small since the film thickness values at probes 4, 5, 6 and 7 are 1.34 mm, 1.18 mm, 1.06 mm, and 1.27 mm respectively.
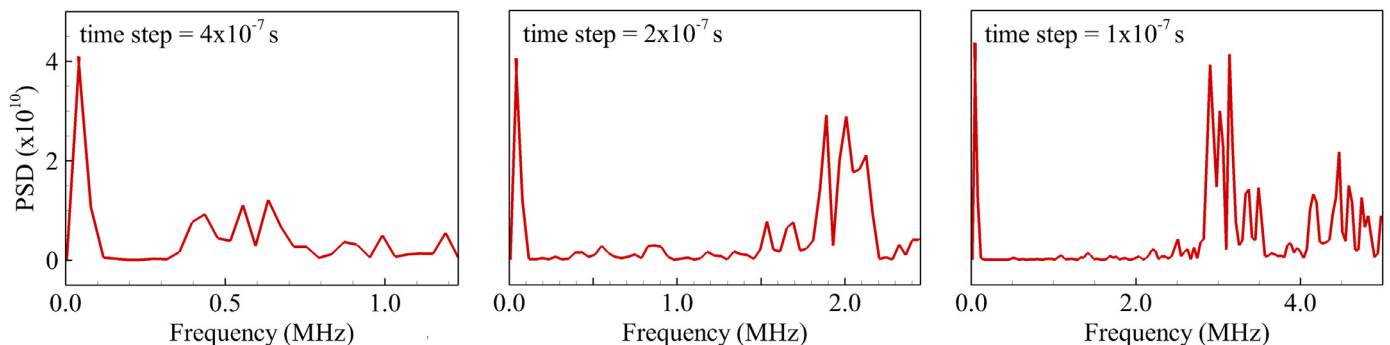

Fig. 13. Power spectral densities for different sampling time step sizes.
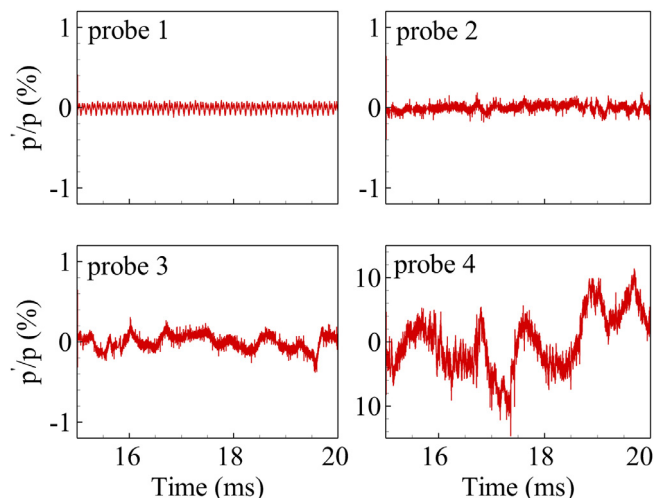
Fig. 14. Time histories of pressure fluctuations at various longitudinal probe locations.
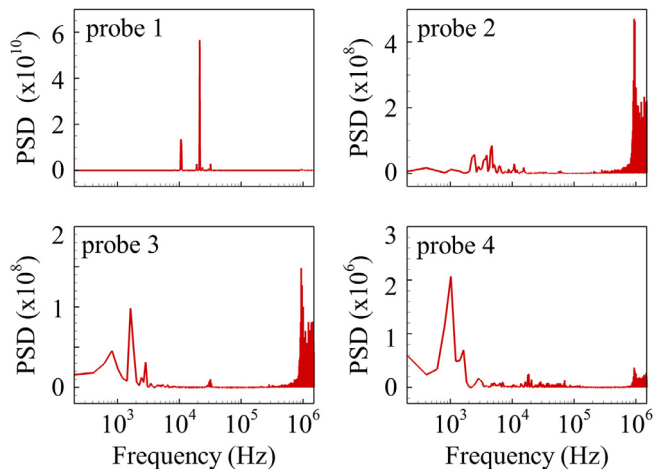

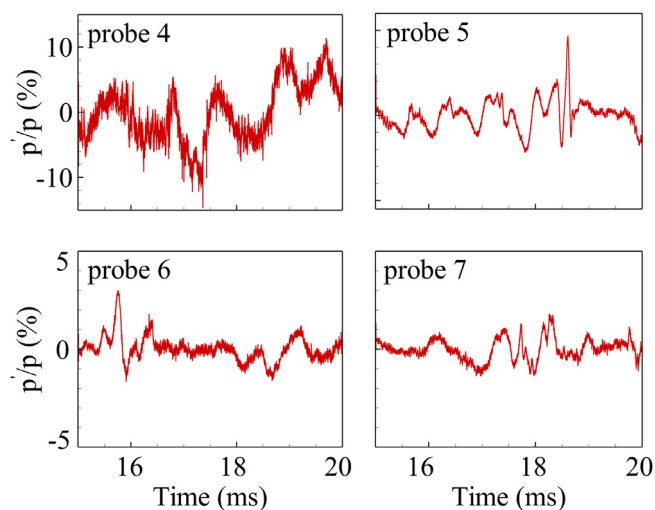Fig. 15. Power spectral densities of pressure fluctuations at various longitudinal probe locations.

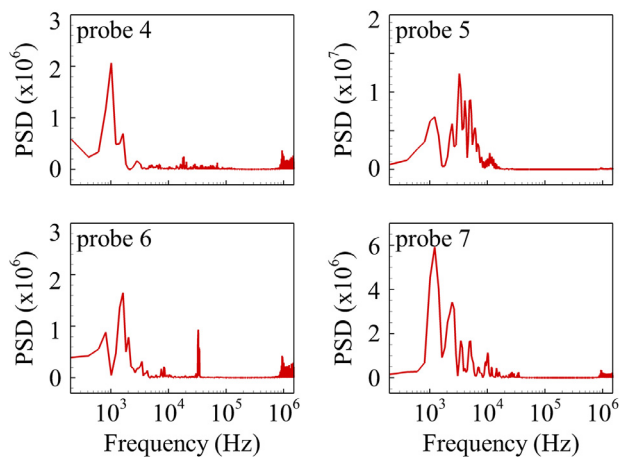Fig. 16. Time histories of pressure fluctuations at various circumferential probe locations.

Fig. 17. Power spectral densities of pressure fluctuations at various circumferential probe locations.

4. Concluding remarks

A numerical study was carried out to investigate the three-dimensional flow dynamics of an open-type swirl injector. The interFoam solver in OpenFOAM was used for multiphase flow simulations. The computational framework employs the LES technique with a one-equation eddy-viscosity subgrid model for turbulence modeling, and the VOF method for capturing the gas-liquid interface. The mesh resolution required to obtain converged flowfield quantities was identified through a grid convergence study. The numerical results obtained with the current computational setup show good agreement with experimental results.

The three-dimensional multiphase flow characteristics are presented at different locations inside the injector. It is observed that the helical flow field inside the injector is not smooth, but has a wavy structure. The smoothness of the flow field decreases as we move toward the exit of the injector. A helical air core is formed inside the injector, which damps the pressure waves propagating from the combustion chamber to the feed system. A triple helix-shaped edge is seen swirling along the air core, due to the presence of three tangential inlets that feed the liquid into the swirl chamber. The helical air core and the liquid film are asymmetric with respect to the center of the chamber. The liquid spray outside the injector is examined in detail to describe the liquid jet breakup and atomization processes. An almost conical spray pattern is found outside the injector. Surface waves formed on the conical spray are turbulent and cause the liquid jet to breakup. The variation in film thickness has an important influence on the liquid film breakup and atomization processes. The atomization process in which the liquid film breaks into ligaments, which then break down into primary and secondary droplets, is also discussed in this study.

The unsteady dynamics of the injector are quantified in detail using spectral analysis. The high frequency pressure oscillations inside the injector decay as the flow reaches the exit of the injector. The spectral characteristics of the liquid film at the exit of the injector vary in the circumferential direction, leading to asymmetries in the subsequently formed spray cone and droplet distributions. This paper lays the foundation for more detailed studies of open-type swirl injectors, and future investigation of the effects of different swirl chamber geometries.

Authorship contributions

Conception and design of study: V. Natarajan, W.-S. Hwang, J.-Y. Choi.

Acquisition of data: V. Natarajan, W.-S. Hwang.

Analysis and/or interpretation of data: V. Natarajan, J.-Y. Choi.

Drafting the manuscript: V. Natarajan, W.-S. Hwang, J.-Y. Choi revising the manuscript critically for important intellectual content:

V. Natarajan, U. Unnikrishnan, V. Yang, J.-Y. Choi.

Approval of the version of the manuscript to be published (the names of all authors must be listed):

V. Natarajan, W.-S. Hwang, U. Unnikrishnan, V. Yang, J.-Y. Choi.

Declaration of Competing Interest

The authors declare that they have no known competing financial interests or personal relationships that could have appeared to influence the work reported in this paper.

Acknowledgements

References

Abramovich, G.N., 1944. The theory of swirl atomizers. Industrial Aerodynamics. BNT ZAGI, Moscow, Russia.

Amini, G., 2016. Liquid flow in a simplex swirl nozzle. Int. J. Multiphase Flow 79, 225–235.

Anderson, W.E., Yang, V., 1995. Liquid Rocket Engine Combustion Instability. American Instiute of Aeronautics and Astronautics.

Bai, X., Sheng, L., Li, Q., Cheng, P., Kang, Z., 2020. Effects of annulus width and post thickness on self-pulsation characteristics for Liquid-Centered Swirl Coaxial Injectors. Int. J. Multiphase Flow 122, 103140.

Balabel, A., 2012. Numerical modeling of turbulence-induced interfacial instability in two-phase flow with moving interface. Appl. Math. Modell. 36, 3593–3611.

Bazarov, V., 1996. Influence of propellant injector stationary and dynamic parameters on high frequency combustion stability. 32nd Joint Propulsion Conference and Exhibit. AIAA 1996-3119.

Bazarov, V., Yang, V., Puri, P., 2004. Design and Dynamics of Jet and Swirl Injectors, Liquid Rocket Thrust Chambers. American Institute of Aeronautics and Astronautics, pp. 19–103.

Bazarov, V.G., Yang, V., 1998. Liquid-propellant rocket engine injector dynamics. J. Propul. Power 14, 797–806.

Charalampous, G., Hadjiyiannis, C., Hardalupas, Y., 2016. Comparative measurement of the breakup length of liquid jets in airblast atomisers using optical connectivity, electrical connectivity and shadowgraphy. Measurement 89, 288–299.

Chen, X., Yang, V., 2014. Effect of ambient pressure on liquid swirl injector flow dynamics. Phys. Fluids 26, 102104.

Cheng, P., Li, Q., Chen, H., Kang, Z., 2018. Study on the dynamic response of a pressure swirl injector to ramp variation of mass flow rate. Acta Astronaut. 152, 449–457.

Chinn, J.J., Cooper, D., Yule, A.J., Nasr, G.G., 2016. Stationary rotary force waves on the liquid–air core interface of a swirl atomizer. Heat Mass Transf 52, 2037–2050.

Chung, Y., Kim, H., Jeong, S., Yoon, Y., 2016. Dynamic characteristics of open-type swirl injector with varying geometry. J. Propul. Power 32, 583–591.

Cossali, G.E., Coghe, A., Marengo, M., 1997. The impact of a single drop on a wetted solid surface. Exp. Fluids 22, 463–472.

Culick, F.E.C., Yang, V., 1995. Overview of combustion instabilities in liquid-propellant rocket engines. Liquid Rocket Engine Combustion Instability. American Institute of Aeronautics and Astrophysics.

Dash, S.K., Halder, M.R., Peric, M., Som, S.K., 2001. Formation of air core in nozzles with tangential entry. J. Fluids Eng. 123, 829–835.

Deshpande, S.S., Lakshman, A., Mario, F.T., 2012. Evaluating the performance of the two-phase flow solver interFoam. Comput. Sci. Discov. 5.

Ding, J.-W., Li, G.-X., Yu, Y.-S., Li, H.-M., 2016. Numerical investigation on primary atomization mechanism of hollow cone swirling sprays. Int. J. Rotating Mach. 2016.

Elbadawy, I., Gaskell, P.H., Lawes, M., Thompson, H.M., 2015. Numerical investigation of the effect of ambient turbulence on pressure swirl spray characteristics. Int. J. Multiphase Flow 77, 271–284.

Fu, Q.-F., 2015. Numerical simulation of the internal flow of swirl atomizer under ambient pressure. Proc. Inst. Mech. Eng. Part C J. Mech. Eng. Sci. 230, 2650–2659.

Fu, Q.-F., Ge, F., Wang, W., Yang, L.-J., 2019. Spray characteristics of gel propellants in an open-end swirl injector. Fuel 254, 115555.

Fu, Q.-F., Yang, L.-J., Qu, Y.-Y., 2011a. Measurement of annular liquid film thickness in an open-end swirl injector. Aerosp. Sci. Technol. 15, 117–124.

Fu, Q.-F., Yang, L.-J., Qu, Y.-Y., Gu, B., 2011b. Geometrical effects on the fluid dynamics of an open-end swirl injector. J. Propul. Power 27, 929–936.

Fu, Q.-F., Yang, L.-J., Wang, X.-D., 2010. Theoretical and experimental study of the dynamics of a liquid swirl injector. J. Propul. Power 26, 94–101.

Fu, Q.-F., Yang, L.-J., Zhang, W., Cui, K.-D., 2012. Spray characteristics of an open-end swirl injector. At. Sprays. 22, 431–445.

Fuster, D., Bagué, A., Boeck, T., Le Moyne, L., Leboissetier, A., Popinet, S., Ray, P., Scardovelli, R., Zaleski, S., 2009. Simulation of primary atomization with an octree adaptive mesh refinement and VOF method. Int. J. Multiphase Flow 35, 550–565.

Galbiati, C., Ertl, M., Tonini, S., Cossali, G.E., Weigand, B., 2016a. DNS Investigation of the Primary Breakup in a Conical Swirled Jet, High Performance Computing in Science and Engineering '15. Springer International Publishing, Cham, pp. 333–347.

Galbiati, C., Tonini, S., Conti, P., Cossali, G.E., 2016b. Numerical simulations of internal flow in an aircraft engine pressure swirl atomizer. J. Propul. Power 32, 1433–1441.

Harrje, D.T., Reardon, F.H., 1972. Liquid Propellant Rocket Combustion Instability. Scientific and Technical Information Office, National Aeronautics and Space Administration,, U.S. Govt Print. Off.

Hulka, J., Makel, D., 1993. Liquid oxygen/hydrogen testing of a single swirl coaxial injector element in a windowed combustion chamber. 29th Joint Propulsion Conference and Exhibit. AIAA 1993–1954.

Hulka, J., Schneider, J., 1993. Single element injector cold flow testing for STME swirl coaxial injector element design. 29th Joint Propulsion Conference and Exhibit. AIAA 1993–2161.

Hulka, J., Schneider, J., Dexter, C., 1991. Performance and stability of a booster class LOX/hydrogen swirl coaxial-element injector. 27th Joint Propulsion Conference. AIAA 1991–1877.

Huo, H., Zong, N., Yang, V., 2009. Cryogenic fluid dynamic response of swirl injector to external forcing at supercritical conditions. 47th AIAA Aerospace Sciences Meeting including The New Horizons Forum and Aerospace Exposition. AIAA 2009-233.

Im, J.-H., Kim, D., Yoon, Y., Roh, T., Koo, J., 2005. Self-pulsation characteristics of a swirl coaxial injector with various injection and geometric conditions. 41st AIAA/ASME/SAE/ASEE Joint Propulsion Conference & Exhibit. AIAA 2005-3749.

Inamura, T., Tamura, H., Sakamoto, H., 2003. Characteristics of liquid film and spray injected from swirl coaxial injector. J. Propul. Power 19, 632–639.

Ismailov, M., Heister, S.D., 2011a. Dynamic response of rocket swirl injectors, part I: wave reflection and resonance. J. Propul. Power 27, 402–411.

Ismailov, M., Heister, S.D., 2011b. Dynamic response of rocket swirl injectors, part ii: nonlinear dynamic response. J. Propul. Power 27, 412–421.

Kenny, R.J., Hulka, J.R., Moser, M.D., Rhys, N.O., 2009. Effect of chamber backpressure on swirl injector fluid mechanics. J. Propul. Power 25, 902–913.

Khavkin, Y., 2004. The Theory and Practice of Swirl Atomizers. Taylor & Francis, New York.

Kim, D., Im, J.-H., Koh, H., Yoon, Y., 2007. Effect of ambient gas density on spray characteristics of swirling liquid sheets. J. Propul. Power 23, 603–611.

Kim, H., 2014. Experimental Study on the Dynamic Characteristics of Open Type Swirl Injector with Varying Geometry M.S. Thesis. School of Mechanical and Aerospace Engineering. Seoul National University.

Kim, J.G., Han, Y.M., Choi, H.S., Yoon, Y., 2013. Study on spray patterns of gas-centered swirl coaxial (GCSC) injectors in high pressure conditions. Aerosp. Sci. Technol. 27, 171–178.

Kim, W.-W., Menon, S., 1995. A new dynamic one-equation subgrid-scale model for large eddy simulations. 33rd Aerospace Sciences Meeting and Exhibit. AIAA 1995-356.

Kolev, N.I., 2012. Introduction to turbulence of multi-phase flows. In: Kolev, N.I. (Ed.), Multiphase Flow Dynamics 4: Turbulence, Gas Adsorption and Release, Diesel Fuel Properties. Springer Berlin, Heidelberg, Berlin, pp. 39–65.

Laurila, E., Koivisto, S., Kankkunen, A., Saari, K., Maakala, V., Järvinen, M., Vuorinen, V., 2020. Computational and experimental investigation of a swirl nozzle for viscous fluids. Int. J. Multiphase Flow 128, 103278.

Laurila, E., Roenby, J., Maakala, V., Peltonen, P., Kahila, H., Vuorinen, V., 2019. Analysis of viscous fluid flow in a pressure-swirl atomizer using large-eddy simulation. Int. J. Multiphase Flow 113, 371–388.

Long, M., Bazarov, V., Anderson, W., 2003. Main chamber injectors for advanced hydrocarbon booster engines. 39th AIAA/ASME/SAE/ASEE Joint Propulsion Conference and Exhibit. AIAA 2003-5499.

Mandal, A., Jog, M.A., Xue, J., Ibrahim, A.A., 2008. Flow of power-law fluids in simplex atomizers. Int. J. Heat Fluid Flow 29, 1494–1503.

Moon, Y., Kim, D., Yoon, Y., 2010. Improved spray model for viscous annular sheets in a swirl injector. J. Propul. Power 26, 267–279.

Nouri-Borujerdi, A., Kebriaee, A., 2012. Numerical simulation of laminar and turbulent two-phase flow in pressure-swirl atomizers. AIAA J. 50, 2091–2101.

Rahman, S., Pal, S., Santoro, R., 1995. Swirl coaxial atomization - cold-flow and hot–fire experiments. 33rd Aerospace Sciences Meeting and Exhibit. AIAA 1995-381.

Renze, P., Heinen, K., Schönherr, M., 2011. Experimental and numerical investigation of pressure swirl atomizers. 34, 1191–1198.

Santolaya, J.L., García, J.A., Calvo, E., Cerecedo, L.M., 2013. Effects of droplet collision phenomena on the development of pressure swirl sprays. Int. J. Multiphase Flow 56, 160–171.

Sasaki, M., Sakamoto, H., Takahashi, M., Tomita, T., Tamura, H., Sasaki, M., Sakamoto, H., Takahashi, M., Tomita, T., Tamura, H., 1997. Comparative study of recessed and non-recessed swirl coaxial injectors. 33rd Joint Propulsion Conference and Exhibit. AIAA 1997-2907.

Shao, C., Luo, K., Yang, Y., Fan, J., 2017. Detailed numerical simulation of swirling primary atomization using a mass conservative level set method. Int. J. Multiphase Flow 89, 57–68.

Shirani, E., Jafari, A., Ashgriz, N., 2006. Turbulence models for flows with free surfaces and interfaces. AIAA J. 44, 1454–1462.

Siamas, G.A., Jiang, X., Wrobel, L.C., 2009. Dynamics of annular gas–liquid two-phase swirling jets. Int. J. Multiphase Flow 35, 450–467.

Smagorinsky, J., 1963. General circulation experiments with the primitive equations: I. The basic experiment. Monthly Weather Rev. 91, 99–164.

Som, S.K., Mukherjee, S.G., 1980. Theoretical and experimental investigations on the formation of air core in a swirl spray atomizing nozzle. Appl. Sci. Res. 36, 173–196.

Taylor, G., 1948. The mechanism of swirl atomizers. In: Proceedings of the 7th International Congress for Applied Mechanics. London.

Wang, S., Hsieh, S.-Y., Yang, V., 2001. Numerical simulation of gas turbine swirl-stabilized injector dynamics. 39th Aerospace Sciences Meeting and Exhibit. AIAA 2001-0334.

Wang, S., Yang, V., Hsiao, G., Hsieh, S.-Y., Mongia, H.C., 2007. Large-eddy simulations of gas-turbine swirl injector flow dynamics. J. Fluid Mech. 583, 99–122.

Wang, X., Huo, H., Wang, Y., Yang, V., 2017a. Comprehensive study of cryogenic fluid dynamics of swirl injectors at supercritical conditions. AIAA J. 55, 3109–3119.

Wang, X., Huo, H., Wang, Y., Zhang, L., Yang, V., 2015. A three-dimensional analysis of swirl injector flow dynamics at supercritical conditions. 53rd AIAA Aerospace Sciences Meeting. AIAA 2015-1827.

Wang, X., Wang, Y., Yang, V., 2017b. Geometric effects on liquid oxygen/kerosene bi-swirl injector flow dynamics at supercritical conditions. AIAA J. 55, 3467–3475.

Wang, X., Wang, Y., Yang, V., 2019. Three-dimensional flow dynamics and mixing in a gas-centered liquid-swirl coaxial injector at supercritical pressure. Phys. Fluids 31, 065109.

Wu, P.K., Ruff, G., Faeth, G., 1991. Primary breakup in liquid/gas mixing layers. 29th Aerospace Sciences Meeting. AIAA 91-19219.

Wu, P.K., Tseng, L.K., Faeth, G., 1992. Primary breakup in gas/liquid mixing layers for turbulent liquids. 30th Aerospace Sciences Meeting and Exhibit. AIAA 92-0462.

Yeh, C.-L., 2007a. Numerical simulation of a turbulent liquid jet emanating from a plain-orifice atomizer and a pressure-swirl atomizer. Numer. Heat Transf. Part A 51, 1187–1212.

Yeh, C.-L., 2007b. Turbulent flow simulation of liquid jet emanating from pressure-swirl atomizer. Heat Mass Transf. 44, 275.

Zhang, L., Wang, X., Li, Y., Yeh, S.-T., Yang, V., 2018. Supercritical fluid flow dynamics and mixing in gas-centered liquid-swirl coaxial injectors. Phys. Fluids 30, 075106.

Zong, N., Yang, V., 2008. Cryogenic fluid dynamics of pressure swirl injectors at supercritical conditions. Phys. Fluids 20, 056103.